

Ephemeral Antibubbles: Spatiotemporal Evolution from Direct Numerical Simulations

Nairita Pal,¹ Rashmi Ramadugu,² Prasad Perlekar,² and Rahul Pandit³

¹*Los Alamos National Laboratory, NM 87545, USA*

²*TIFR Center for Interdisciplinary Sciences, Tata Institute of Fundamental Research, Gopanally, Hyderabad, 500046, India*

³*Centre for Condensed Matter Theory, Department of Physics,*

Indian Institute of Science, Bangalore 560012, India

(Dated: April 1, 2021)

Antibubbles, which consist of a shell of a low-density fluid inside a high-density fluid, have several promising applications. We show, via extensive direct numerical simulations (DNSs), in both two and three dimensions (2D and 3D), that the spatiotemporal evolution of antibubbles can be described naturally by the coupled Cahn-Hilliard-Navier-Stokes (CHNS) equations for a binary fluid. Our DNSs capture elegantly the gravity-induced thinning and breakup of an antibubble via the time evolution of the Cahn-Hilliard scalar order parameter field ϕ , which varies continuously across interfaces, so we do not have to enforce complicated boundary conditions at the moving antibubble interfaces. To ensure that our results are robust, we supplement our CHNS simulations with sharp-interface Volume-of-Fluid (VoF) DNSs. We track the thickness of the antibubble and calculate the dependence of the lifetime of an antibubble on several parameters; we show that our DNS results agree with various experimental results; in particular, the velocity with which the arms of the antibubble retract after breakup scales as $\sigma^{1/2}$, where σ is the surface tension.

I. INTRODUCTION

Antibubbles, which comprise a shell of a low-density fluid inside a high-density fluid, have been known for close to 90 years, since the work of Hughes and Hughes [1]. In contrast to an ordinary bubble, an antibubble has two surfaces, which trap a certain volume of fluid between them. Therefore, the contact area of an antibubble is much larger than that of a bubble with the same fluid volume; this property can be exploited for a variety of chemical reactions. Furthermore, antibubbles are commonly used in clinical diagnostic imaging, sonoporation (see, e.g., Ref. [2]), as agents for ultrasound-guided drug delivery [3–5], and for active leakage detection [6]. Clearly, an antibubble is unstable in the presence of gravity, and, if the inner core of the antibubble is denser than the outer core, the antibubble rises under gravity; because of hydrostatic pressure in the outer core, the fluid rises from the bottom to the top, resulting in a thinning, and subsequent collapse, of the outer shell. Although there have been a number of experimental investigations of the spatiotemporal evolution of an antibubble [7–15] and drops [16–20] to name a few, over the past few decades, theoretical studies of antibubble evolution have been initiated only recently [15, 21–25] and they have not, attempted, hitherto, to address the spatiotemporal evolution of antibubbles in detail. The number of experimental studies of the complete spatiotemporal evolution of antibubbles is also limited, partly because great care has to be exercised to stabilise antibubbles; often, surfactant molecules have to be introduced into the high-density liquid phase for such stabilization.

We develop a *natural, multiphase* model for antibubbles and demonstrate how we can use direct numerical simulations (DNSs) to follow the spatiotemporal development of ephemeral, but beautiful, antibubbles. We show that the Cahn-Hilliard-Navier-Stokes (CHNS) equations,

which have been used to study a variety of problems in binary-fluid flows [26–35], provide a *minimal theoretical framework* for studying the spatiotemporal evolution of antibubbles; in addition to a velocity field, the CHNS system employs a phase field ϕ that distinguishes between the two fluid phases. We use the CHNS equations [26, 27, 29–32] to study antibubbles in two-dimensions (2D) and in three dimensions (3D) by using extensive DNSs. To complement our CHNS results, we also employ an alternative Volume-of-Fluid (VoF) numerical scheme that is a sharp-interface method.

Our studies yield several interesting results that (a) provide explanations for many experimental observations and (b) suggest new experimental studies: Our results for the spatiotemporal evolution of antibubbles, in 2D and 3D, show clearly how antibubble breakup occurs either because of gravity-induced thinning or the puncturing of its bottom boundary; the the collapsing antibubble then forms a rim that retracts with a velocity v_{rim} . We uncover signatures of this collapse in Fourier-space spectra of the Cahn-Hilliard field ϕ , the velocity, and the vorticity. We show that $v_{rim} \sim \sigma^{1/2}$, where σ is the surface tension; and this power-law exponent is independent of the kinematic viscosity ν of the background fluid. We investigate the dependence of the scaled antibubble lifetime τ_1/τ_g on σ , ν , and the scaled outer radius of the antibubble R_0/h_0 , in 2D; here, $\tau_g \equiv \sqrt{R_0/Ag}$, with A the Atwood number and g the acceleration due to gravity, and h_0 is the initial thickness of the antibubble shell. We compare our results with experiments and earlier theoretical studies.

The remainder of this paper is organized as follows: In Sec. II we present the models and the numerical methods that we use. In Sec. III we present the results our DNSs in the following subsections:

- subsection III A on the spatiotemporal evolution of antibubbles (2D DNSs);

- subsection IIIB on the temporal evolution of Fourier spectra of ϕ and the velocity and vorticity fields that are associated with antibubbles in our 2D DNSs;
- subsection IIIC on the velocity of the retracting rim of the ruptured antibubble in our 2D DNSs;
- subsection IIID on the signatures of this rupture in the time dependence of the energy;
- subsection IIIE1 on the dependence of the antibubble-rupture time on the size of the antibubble and the surface tension;
- subsection IIIE2 on the dependence of the antibubble-rupture time on the kinematic viscosity;
- subsection IIIF on the spatiotemporal evolution of antibubbles in our 3D DNSs.

We present conclusions and a discussion of our results in Sec. IV.

II. MODEL AND NUMERICAL METHODS

An antibubble consists of a shell of light fluid of density ρ_1 inside a background heavy fluid of density ρ_2 ; these fluids are immiscible and incompressible. The following CHNS equations provide a natural theoretical description for such a binary-fluid mixture [36–39]:

$$\rho(\phi)D_t\mathbf{u} = -\nabla p + \zeta(\phi)\nabla^2\mathbf{u} + \mathbf{F}_\sigma + [\rho(\phi) - \frac{\rho_1 + \rho_2}{2}]\mathbf{g} - \alpha\mathbf{u}; \quad (1)$$

$$D_t\phi = \gamma\nabla^2\mu \text{ and } \nabla \cdot \mathbf{u} = 0; \quad (2)$$

In Eqs.(1)-(2), $D_t \equiv (\partial_t + \mathbf{u} \cdot \nabla)$ is the convective derivative, $\mathbf{u} \equiv (u_x, u_y, u_z)$ is the fluid velocity, α is the coefficient of friction (we use this only in 2D), \mathbf{g} is the constant acceleration due to gravity, which points downwards, $\rho(\phi) \equiv \rho_1(1 + \phi)/2 + \rho_2(1 - \phi)/2$ is the density, $\zeta(\phi) \equiv \nu_1(1 + \phi)/2 + \nu_2(1 - \phi)/2$ is the dynamic viscosity, $\phi(\mathbf{x}, t)$ is the order-parameter field at the point \mathbf{x} and time t [with $\phi(\mathbf{x}, t) > 0$ in the background (majority) phase and $\phi(\mathbf{x}, t) < 0$ in the antibubble-shell (minority) phase]. For the illustrative results that we present, we choose $\rho(\phi)$ and $\zeta(\phi)$ such that the kinematic viscosity ν is identical in the two phases.

When we study 2D flows, we use the following streamfunction-vorticity formulation [26, 40]:

$$\begin{aligned} (\partial_t + \mathbf{u} \cdot \nabla)\omega &= \nu\nabla^2\omega - \alpha\omega - \nabla \times (\phi\nabla\mu) - A\nabla\phi \times \mathbf{g}; \\ (\partial_t + \mathbf{u} \cdot \nabla)\phi &= \gamma\nabla^2\mu \text{ and } \nabla \cdot \mathbf{u} = 0. \end{aligned} \quad (3)$$

Here, $\omega = (\nabla \times \mathbf{u})\hat{e}_z$ is the vorticity. We obtain $\omega(\mathbf{x}, t)$ and $\phi(\mathbf{x}, t)$ from our 2D DNS [41], and from these we calculate the total kinetic energy $E(t) = \langle |\mathbf{u}(\mathbf{x}, t)|^2 \rangle_{\mathbf{x}}$ and

the fluid-energy dissipation rate $\varepsilon(t) = \langle \nu|\omega(\mathbf{x}, t)|^2 \rangle_{\mathbf{x}}$, where $\langle \rangle_{\mathbf{x}}$ denotes the average over space, and $\omega = \nabla \times \mathbf{u}$ is the fluid vorticity. We calculate the lifetime of an antibubble falling under gravity in two ways: (a) from the energy time series; and (b) from the minimum thickness at the South pole of the antibubble.

At time $t = 0$ we begin with the order-parameter profile [36]

$$\begin{aligned} \phi(\mathbf{x}) &= -\tanh\left[\frac{1}{\sqrt{2}\xi}(|\mathbf{x} - \mathbf{x}_c| - R_0)\right] \\ &+ \tanh\left[\frac{1}{\sqrt{2}\xi}(|\mathbf{x} - \mathbf{x}_c| - R_1)\right] - 1.0, \end{aligned} \quad (4)$$

where R_0 and R_1 are, respectively, the initial magnitudes of the outer and inner radii of the antibubble, whose centre is initially at \mathbf{x}_c ; the interface width ξ is measured by the dimensionless Cahn number $Ch = \xi/L$. We use the initial thickness of the antibubble shell $h_0 \equiv R_0 - R_1$ as a typical length scale.

In our CHNS studies we use the Boussinesq approximation, wherein $\rho(\phi)D_t\mathbf{u} \approx \frac{\rho_1 + \rho_2}{2}D_t\mathbf{u}$ and $[\rho(\phi) - \frac{\rho_1 + \rho_2}{2}]\mathbf{g} \approx -A\phi\mathbf{g}$ in Eq.(1); the surface-tension force $\mathbf{F}_\sigma \equiv -\phi\nabla\mu$ and the chemical potential $\mu(\mathbf{x}, t)$ follow from the Cahn-Hilliard free-energy functional \mathcal{F} (see the Supplemental Material [41]):

$$\begin{aligned} \mu &= \delta\mathcal{F}[\phi]/\delta\phi(\mathbf{x}, t); \\ \mathcal{F}[\phi] &= \Lambda \int [(\phi^2 - 1)^2/(4\xi^2) + |\nabla\phi|^2/2]d\mathbf{x}; \end{aligned} \quad (5)$$

here, Λ is the energy density with which the two phases mix in the interfacial regime [36], ξ sets the scale of the interface width, $\sigma = \frac{2\sqrt{2}\Lambda}{3\xi}$ is the surface tension, γ is the mobility [38] of the binary-fluid mixture; the Cahn number $Ch = \xi/L$, where L is the linear size of our simulation domain, is a dimensionless measure of the interfacial width; the Schmidt number $Sc = \nu/D$. We assume that γ and ρ are independent of ϕ ; we keep the diffusivity $D = \frac{\gamma\Lambda}{\xi^2}$ constant. We study the retraction dynamics of an antibubble by varying the Atwood number $A = (\rho_2 - \rho_1)/(\rho_2 + \rho_1)$ and the Bond number $Bo = Ag\rho h_0^2/\sigma$. The Bond number is a convenient dimensionless ratio of body forces (gravity), on the antibubble, and the surface or interfacial tension σ . We express times in multiples of $\tau_g \equiv \sqrt{R_0/Ag} = 1.16$.

We solve the CHNS Eqs.(1)-(2) by using the pseudospectral method with periodic boundary conditions; because of the cubic nonlinearity in the chemical potential μ , we use $N/2$ -dealiasing [42]. We use the exponential Adams-Bashforth method ETD2 [43] for time marching. For our 2D DNSs, we use computers with Graphics Processing Units (e.g., the NVIDIA K80), which we program in CUDA [44]. We use conventional CPU-based computers for our 3D DNSs. We have N collocation points in each direction, and our domain length is $L = 2\pi$. Our efficient code allows us to explore the CHNS parameter

space and carry out very long simulations that are essential for our studies.

For the VoF method we note the following points: It is a sharp-interface method, so it has $Ch = 0$. The surface tension force for VoF is $\mathbf{F}_\sigma \equiv \sigma \kappa \delta_s \mathbf{n}$, where κ is the curvature, δ_s is the Dirac delta function on the interface, and \mathbf{n} is the normal to the interface. We use Basilisk [45, 46], an open-source solver for carrying out both 2D and 3D axisymmetric VoF DNSs. Basilisk, which employs the Bell-Collela-Glaz advection scheme [47] and the implicit viscosity solver [45, 46], is parallelized over conventional CPUs [45, 46]. The VoF solver does not invoke the Boussinesq approximation; and it can handle large density and viscosity contrasts. The breakup of an interface is sensitive to the resolution in the VoF, so we use an initial configuration in which the antibubble is already punctured at the bottom; and we then investigate its spatiotemporal evolution. This initial condition is similar to that used in experiments and in Ref. [23]. We use the following boundary conditions in our VoF simulations: (a) In our 2D DNSs we employ periodic boundary conditions in all directions; (b) in the 3D axisymmetric case we use an axisymmetric boundary condition on the $z = 0$ axis and the no-slip condition $\mathbf{u} = 0$ at other boundaries.

We list the parameters for some of our representative DNS runs in Tables I, II, III, and IV. We also give Tables with the details of all our DNSs in the Supplemental Material [41]. As we show below, by utilising both the CHNS framework and the VoF method, we can capture accurately the rupture and retraction dynamics of an antibubble in an elegant and numerically efficient way.

III. RESULTS

We now present the results of our DNSs in the following subsections: In subsection III A we illustrate the spatiotemporal evolution of 2D antibubbles and, in subsection III B, we give the temporal evolution of Fourier spectra of ϕ and the velocity and vorticity fields that are associated with these antibubbles. In subsection III C we explore the dependence on σ of the velocity of the retracting rim of a ruptured 2D antibubble; and, in subsection III D, we examine the signatures of this rupture in the time dependence of the energy. Furthermore, we elucidate the dependence of the antibubble-rupture time on the size of the antibubble and the surface tension (subsection III E 1) and on the kinematic viscosity (subsection III E 2). We then present illustrative results on the spatiotemporal evolution of 3D antibubbles in subsection III F

A. Spatiotemporal evolution: 2D

In Fig. 1 we display, via pseudocolor plots of ϕ and ω , the spatiotemporal evolution of a 2D antibubble rising under gravity in our CHNS DNS; blue and red indicate

	N	R_0/ξ	R_1/ξ	R_0/h_0	h_0/ξ	D	Ch	$Bo(\times 10^{-3})$	ν	Sc
R1	1024 (2D)	76.6	69.7	7	6.96	0.004	0.0028	36	0.007	1.75
R2	1024 (2D)	76.6	69.7	7	6.96	0.004	0.0028	12	0.007	1.75
R3	1024 (2D)	76.6	69.7	7	6.96	0.004	0.0028	8.9	0.007	1.75
R4	1024 (2D)	76.6	69.7	7	6.96	0.004	0.0028	5.0	0.007	1.75
R5	1024 (2D)	76.6	69.7	7	6.96	0.004	0.0028	4.0	0.007	1.75
R6	1024 (2D)	76.6	69.7	7	6.96	0.004	0.0028	4.5	0.007	1.75
R7	1024 (2D)	76.6	69.7	7	6.96	0.004	0.0028	3.3	0.007	1.75
R8	1024 (2D)	76.6	69.7	7	6.96	0.004	0.0028	2.7	0.007	1.75
R9	1024 (2D)	76.6	69.7	7	6.96	0.004	0.0028	2.4	0.007	1.75
R10	1024 (2D)	76.6	69.7	7	6.96	0.004	0.0028	2.1	0.007	1.75
R11	1024 (2D)	76.6	69.7	7	6.96	0.004	0.0028	1.9	0.007	1.75
R12	1024 (2D)	76.6	69.7	7	6.96	0.004	0.0028	1.7	0.007	1.75
R13	1024 (2D)	76.6	69.7	7	6.96	0.004	0.0028	1.5	0.007	1.75
R14	1024 (2D)	76.6	69.7	7	6.96	0.004	0.0028	1.4	0.007	1.75
R15	1024 (2D)	76.6	69.7	7	6.96	0.004	0.0028	1.3	0.007	1.75
R16	1024 (2D)	76.6	69.7	7	6.96	0.004	0.0028	1.1	0.007	1.75
R17	1024 (2D)	76.6	69.7	7	6.96	0.004	0.0028	0.8	0.007	1.75
R18	1024 (2D)	76.6	69.7	7	6.96	0.004	0.0028	0.73	0.007	1.75
R19	1024 (2D)	76.6	69.7	7	6.96	0.004	0.0028	0.56	0.007	1.75
R20	1024 (2D)	76.6	69.7	7	6.96	0.004	0.0028	0.45	0.007	1.75
R21	1024 (2D)	76.6	69.7	8	6.96	0.004	0.0028	12	0.007	1.75
R22	1024 (2D)	76.6	69.7	8	6.96	0.004	0.0028	5.0	0.007	1.75
R23	1024 (2D)	76.6	69.7	8	6.96	0.004	0.0028	4.0	0.007	1.75
R24	1024 (2D)	76.6	69.7	8	6.96	0.004	0.0028	3.3	0.007	1.75
R25	1024 (2D)	76.6	69.7	8	6.96	0.004	0.0028	3.1	0.007	1.75
R26	1024 (2D)	76.6	69.7	8	6.96	0.004	0.0028	2.7	0.007	1.75
R27	1024 (2D)	76.6	69.7	8	6.96	0.004	0.0028	2.4	0.007	1.75
R28	1024 (2D)	76.6	69.7	8	6.96	0.004	0.0028	1.9	0.007	1.75
R29	1024 (2D)	76.6	69.7	8	6.96	0.004	0.0028	1.7	0.007	1.75
R30	1024 (2D)	76.6	69.7	8	6.96	0.004	0.0028	1.5	0.007	1.75
R31	1024 (2D)	76.6	69.7	8	6.96	0.004	0.0028	1.3	0.007	1.75
R32	1024 (2D)	76.6	69.7	8	6.96	0.004	0.0028	1.1	0.007	1.75
R33	1024 (2D)	76.6	69.7	8	6.96	0.004	0.0028	0.8	0.007	1.75
R34	1024 (2D)	76.6	69.7	8	6.96	0.004	0.0028	0.73	0.007	1.75
R35	1024 (2D)	76.6	69.7	8	6.96	0.004	0.0028	0.45	0.007	1.75

TABLE I. The parameters $R_0, R_1, h_0, \xi, \sigma, \nu, D, CH, Sc$ for our CHNS DNS runs R1-R35. Initially, R_0 and R_1 are, respectively, the outer and inner radii of the antibubble; $h_0 \equiv (R_0 - R_1)$; σ is the surface tension; ν is the kinematic viscosity. In all the runs, the Atwood number times the acceleration due to gravity $Ag = 0.99$; the number of collocation points is N^2 ; the diffusivity is D ; the Cahn number $Ch = \xi/L$, ξ being the interface width. The typical values of R_0/h_0 used in experiments are about 38 [22]. For all our 2D runs, the friction coefficient $\alpha = 0.001$.

heavy and light fluids, respectively. Figure 1(a) shows the pseudocolor plot of ϕ for the antibubble at a time $\simeq 1.07 \times 0.05\tau_g$. Initially, the antibubble rises because of gravity, breaks (Fig. 1(b)), then displays arms that retract, forms a disc-shaped droplet, which rises under gravity (Fig. 1(c)), because the antibubble-shell (red) fluid is lighter than the background (blue) fluid. Figures 1(d)-(f) show pseudocolor plots of the vorticity field at the same times as their ϕ counterparts in Figs. 1(a)-(c). The spatiotemporal evolution of such a 2D antibubble is shown in the Videos S6 and S7 in the Supplemental Material [41]. Note that, just after forming the disc-type shape, the antibubble goes down in a direction opposite to that dictated by gravity (Fig. 1(e)), because the surface tension is high, so, during the retraction of the

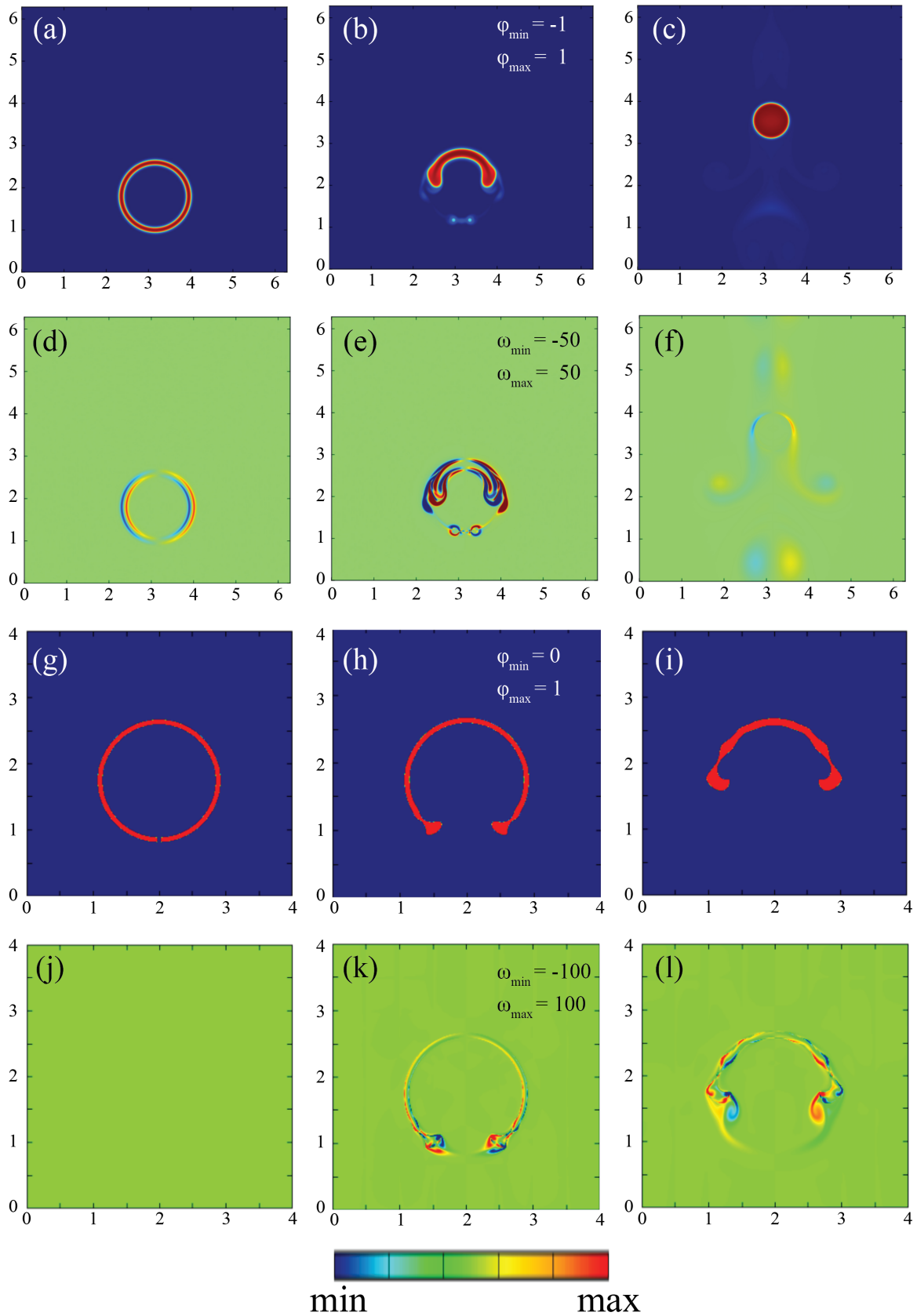


FIG. 1. Pseudocolor plots of the CHNS ϕ field with antibubble radius $R_0/h_0 = 7$ at time (a) $t = 0.05\tau_g$, (b) $t = 3.26\tau_g$, (c) $t = 11.77\tau_g$ for $\nu = 0.007$ and $\sigma = 16.6$ (i.e., $Bo = 0.001$, from our 2D DNS run R16); pseudocolor plots of the corresponding ω field (d)–(f). These plots show that, initially, the antibubble rises under gravity, breaks, (a,d), then it retracts (b,e), becomes a circular droplet and rises again (e,f). Pseudocolor plots of the volume fraction for the 2D VoF run PR5 at time (g) $t = 0$, (h) $t = 0.1\tau_g$, (i) $t = 0.3\tau_g$; (j), (k), and (l) pseudocolor plots of the vorticity for the 2D VoF PR5 run at the same times as in (g), (h), and (i), respectively; in these 2D VoF runs, $\sigma = 1.68$; these plots show that the antibubble retracts and forms a rim. Time is measured in units of τ_g .

	N	R_0/ξ	R_1/ξ	R_0/h_0	h_0/ξ	D	Ch	$Bo(\times 10^{-3})$	ν	Sc
R36	1024 (2D)	76.6	69.7	9	6.96	0.004	0.0028	12	0.007	1.75
R37	1024 (2D)	76.6	69.7	9	6.96	0.004	0.0028	5.0	0.007	1.75
R38	1024 (2D)	76.6	69.7	9	6.96	0.004	0.0028	4.0	0.007	1.75
R39	1024 (2D)	76.6	69.7	9	6.96	0.004	0.0028	3.3	0.007	1.75
R40	1024 (2D)	76.6	69.7	9	6.96	0.004	0.0028	3.1	0.007	1.75
R41	1024 (2D)	76.6	69.7	9	6.96	0.004	0.0028	2.7	0.007	1.75
R42	1024 (2D)	76.6	69.7	9	6.96	0.004	0.0028	2.4	0.007	1.75
R43	1024 (2D)	76.6	69.7	9	6.96	0.004	0.0028	1.9	0.007	1.75
R44	1024 (2D)	76.6	69.7	9	6.96	0.004	0.0028	1.7	0.007	1.75
R45	1024 (2D)	76.6	69.7	9	6.96	0.004	0.0028	1.5	0.007	1.75
R46	1024 (2D)	76.6	69.7	9	6.96	0.004	0.0028	1.3	0.007	1.75
R47	1024 (2D)	76.6	69.7	9	6.96	0.004	0.0028	1.1	0.007	1.75
R48	1024 (2D)	76.6	69.7	9	6.96	0.004	0.0028	0.8	0.007	1.75
R49	1024 (2D)	76.6	69.7	9	6.96	0.004	0.0028	0.73	0.007	1.75
R50	1024 (2D)	76.6	69.7	9	6.96	0.004	0.0028	0.45	0.007	1.75
R51	1024 (2D)	76.6	69.7	11	6.96	0.004	0.0028	0.01	0.007	1.75
R52	1024 (2D)	76.6	69.7	11	6.96	0.004	0.0028	0.01	0.01	2.6
R53	1024 (2D)	76.6	69.7	11	6.96	0.004	0.0028	0.01	0.01	3.9
R54	1024 (2D)	76.6	69.7	11	6.96	0.004	0.0028	0.01	0.02	5.0
R55	1024 (2D)	76.6	69.7	11	6.96	0.004	0.0028	0.01	0.02	6.8
R56	1024 (2D)	76.6	69.7	11	6.96	0.004	0.0028	0.01	0.035	8.75
R57	1024 (2D)	76.6	69.7	11	6.96	0.004	0.0028	0.01	0.035	10.0
R58	1024 (2D)	76.6	69.7	11	6.96	0.004	0.0028	0.01	0.05	12.5
R60	1024 (2D)	76.6	69.7	11	6.96	0.004	0.0028	0.01	0.05	14.0
R61	1024 (2D)	76.6	69.7	11	6.96	0.004	0.0028	0.01	0.05	15.75
R62	1024 (2D)	76.6	69.7	11	6.96	0.004	0.0028	0.01	0.05	17.5
R63	1024 (2D)	76.6	69.7	11	6.96	0.004	0.0028	0.01	0.08	20
R64	1024 (2D)	76.6	69.7	11	6.96	0.004	0.0028	0.01	0.12	30
R65	1024 (2D)	76.6	69.7	11	6.96	0.004	0.0028	0.01	0.18	45
R66	1024 (2D)	76.6	69.7	11	6.96	0.004	0.0028	0.01	0.18	58
R67	1024 (2D)	76.6	69.7	11	6.96	0.004	0.0028	0.01	0.27	67.5
R68	1024 (2D)	76.6	69.7	11	6.96	0.004	0.0028	0.01	0.27	80.0
R69	1024 (2D)	76.6	69.7	11	6.96	0.004	0.0028	0.01	0.4	100
R70	1024 (2D)	76.6	69.7	11	6.96	0.004	0.0028	0.01	0.6	151.5
R71	1024 (2D)	76.6	69.7	11	6.96	0.004	0.0028	0.01	0.96	241.7
R72	1024 (2D)	76.6	69.7	11	6.96	0.004	0.0028	0.1	0.96	241.7

TABLE II. The parameters $R_0, R_1, h_0, \xi, \sigma, \nu, D, CH, Sc$ for our CHNS DNS runs R36-R72. Initially, R_0 and R_1 are, respectively, the outer and inner radii of the antibubble; $h_0 \equiv (R_0 - R_1)$; σ is the surface tension; ν is the kinematic viscosity. In all the runs, the Atwood number times the acceleration due to gravity $Ag = 0.99$, the number of collocation points is N^2 ; the diffusivity is D ; the Cahn number $Ch = \xi/L$, ξ being the interface width. The typical values of R_0/h_0 used in experiments are about 38 [22]. For all our 2D runs, the friction coefficient $\alpha = 0.001$.

arms, when interfacial energy is released, the retracting droplet can be pushed in this opposite direction. Eventually this backward thrust is damped by viscosity and, finally, the (light) droplet rises under gravity. We begin with $\omega = 0$, everywhere. We see that, because of the $\nabla \times \phi \nabla \mu$ term on the right-hand side (RHS) of Eq.(3), a vorticity field is generated at the outer and inner surfaces of the antibubble, i.e., wherever ϕ changes in space. The vortical regions that are generated initially have a size that is comparable to the interface width. These vortices then grow with time, until they are damped by viscosity. Similarly, the gravity term is also significant wherever ϕ changes sign. The competition between the viscous, surface-tension, and gravity terms in the CHNS equations determines the breakup time of an antibubble,

	N	R_0/ξ	R_1/ξ	R_0/h_0	h_0/ξ	D	Ch	$Bo(\times 10^{-3})$	ν	Sc
Q1	256 (3D)	24.0	12.0	1.2	12.0	0.006	0.013	1.3	0.0016	0.27
Q2	256 (3D)	24.0	12.0	1.2	12.0	0.006	0.013	0.63	0.0016	0.27
Q3	256 (3D)	24.0	12.0	1.2	12.0	0.006	0.013	0.4	0.0016	0.27
Q4	256 (3D)	24.0	12.0	1.2	12.0	0.006	0.013	0.3	0.0016	0.27
Q5	256 (3D)	24.0	12.0	1.2	12.0	0.006	0.013	0.25	0.0016	0.27
Q6	256 (3D)	24.0	12.0	1.2	12.0	0.006	0.013	0.21	0.0016	0.27
Q7	512 (3D)	14	10.5	4.0	3.5	0.006	0.011	2.7	0.0016	0.27

TABLE III. The parameters $R_0, R_1, h_0, \xi, \sigma, \nu, D, CH, Sc$ for our CHNS DNS runs Q1-Q7. Initially, R_0 and R_1 are, respectively, the outer and inner radii of the antibubble; $h_0 \equiv (R_0 - R_1)$; σ is the surface tension; ν is the kinematic viscosity. In all the runs, the Atwood number times the acceleration due to gravity $Ag = 0.5$, the number of collocation points is for Q1-Q6 is $N^3 = 256^3$ and for Q7 is $N^3 = 512^3$; the diffusivity is D ; the Cahn number $Ch = \xi/L$, with ξ being the interface width. The typical values of R_0/h_0 used in experiments are about 38 [22].

	R_0	R_1	h_0	A	g	ν	$Bo(\times 10^{-3})$
PR1	0.859	0.739	0.12	0.9	1.	0.007	0.9
PR2	0.859	0.739	0.12	0.9	1.	0.007	1.17
PR3	0.859	0.739	0.12	0.9	1.	0.007	1.82
PR4	0.859	0.739	0.12	0.9	1.	0.007	4.1
PR5	0.859	0.739	0.12	0.9	1.	0.007	8.2
PR6	0.859	0.739	0.12	0.9	1.	0.007	16.4
APR1	0.859	0.739	0.12	0.9	1.	0.007	0.75
APR2	0.859	0.739	0.12	0.9	1.	0.007	0.9
APR3	0.859	0.739	0.12	0.9	1.	0.007	1.17
APR4	0.859	0.739	0.12	0.9	1.	0.007	1.82
APR5	0.859	0.739	0.12	0.9	1.	0.007	2.05
APR6	0.859	0.739	0.12	0.9	1.	0.007	4.1
APR7	0.859	0.739	0.12	0.9	1.	0.007	8.2
APR8	0.859	0.739	0.12	0.9	1.	0.007	16.4
APR9	0.859	0.739	0.12	0.01	100.	0.007	0.9
APR10	0.859	0.739	0.12	0.01	100.	0.007	1.82
APR11	0.859	0.739	0.12	0.01	100.	0.007	2.05
APR12	0.859	0.739	0.12	0.01	100.	0.007	4.1
APR13	0.859	0.739	0.12	0.01	100.	0.007	8.2
APR14	0.859	0.739	0.12	0.01	100.	0.007	16.4

TABLE IV. The parameters R_0, R_1, h_0, A, g, ν and Bo for our VoF runs: 2D(PR1 - PR6); and 3D axisymmetric (APR1 - APR14). For these runs $\rho_2 = 1$. For the 2D and axisymmetric 3D runs we use a square box of area $L^2 = 16$ and discretize it with $N^2 = 2048^2$ collocation points. For our 2D VoF DNSs we employ periodic boundary conditions in all directions; in 3D we use an axisymmetric boundary condition on the $z = 0$ axis and the no-slip boundary condition $\mathbf{u} = 0$ at other boundaries.

as we show below.

In Figs. 1(g)-(l) we use pseudocolor plots to illustrate antibubble retraction in our VoF DNS in 2D (run PR1). Both our CHNS and VoF DNSs show that, as it ruptures, an antibubble forms a rim, which then retracts.

B. Fourier spectra

Fourier-space spectra give us a complementary view of the spatiotemporal evolution of the rupture of an antibubble (cf., the physical-space pseudocolor plots in Figs. 1 (a)-(l)). In Fig. 2 we show, for our 2D CHNS DNSs, log-log (base 10) plots of the spectra for the field ϕ , the energy spectrum $E(k, t)$, and the enstrophy spectrum $\Omega(k, t)$, at different times during this evolution. These spectra are defined as follows:

$$\begin{aligned} S(k, t) &\equiv \sum_{k-\frac{1}{2} \leq k' \leq k+\frac{1}{2}} \langle \hat{\phi}(\mathbf{k}', t) \hat{\phi}(-\mathbf{k}', t) \rangle; \\ E(k, t) &\equiv \frac{1}{2} \sum_{k-\frac{1}{2} \leq k' \leq k+\frac{1}{2}} \langle \hat{\mathbf{u}}(\mathbf{k}', t) \hat{\mathbf{u}}(-\mathbf{k}', t) \rangle; \\ \Omega(k, t) &\equiv \frac{1}{2} \sum_{k-\frac{1}{2} \leq k' \leq k+\frac{1}{2}} \langle \hat{\omega}(\mathbf{k}', t) \hat{\omega}(-\mathbf{k}', t) \rangle; \end{aligned} \quad (6)$$

here, the circumflex denotes a spatial Fourier transform and k and k' are, respectively, the magnitudes of the wave vectors \mathbf{k} and \mathbf{k}' . At early times (Figs. 2 (a), (d), and (g)), these spectra, especially $S(k, t)$, show oscillations with small and large periods, which are, respectively, related inversely to the outer radius of the antibubble and the thickness of its shell. As the antibubble ruptures (Figs. 2 (b), (e), and (h)), it loses its circular shape, and, in turn, the spectra lose their oscillations. Finally, the antibubble is replaced by a single droplet (Fig. 1(c)) of the light fluid, which rises under gravity; at this stage, these spectra, especially $S(k, t)$, show oscillations with a small period, which is related inversely to the radius of this rising droplet. These Fourier-space spectra show that the breakup of an antibubble leads to turbulence, insofar as $E(k, t)$, $S(k, t)$, and $\Omega(k, t)$ extend significantly over several orders of magnitude of k . The Taylor-microscale Reynolds number Re_λ is 0.54, 128.5, and 163.4 in Figs. 2 (a), (b), and (c), respectively; here, $Re_\lambda = u_{rms} \lambda / \nu$, where the root-mean-square velocity $u_{rms}(t) = 2 \sum_k E(k, t)$ and the Taylor microscale $\lambda \equiv [\sum k^2 E(k, t) / \sum E(k, t)]^{-1/2}$.

C. Rim-retraction velocity

When an antibubble ruptures, the surface-tension energy (the interfacial free energy in the CHNS description) is converted to the kinetic energy of the antibubble. The rate of change of the former is $\sigma dS(t)/dt$,

where $S(t)$ is the outer perimeter of the antibubble in our 2D DNSs; and the kinetic energy that is released is $E_M = \int_{S_f} (\rho v^2(\mathbf{x}, t)) d\mathbf{x}$, where S_f is the area of the majority phase surrounding the minority phase; this causes the film to retract. Recall that Figs. 1(a)-(l) show that, in both our CHNS and VoF DNSs, as it ruptures, an antibubble forms a rim, which then retracts. When this rim retracts, the outer perimeter of the antibubble reduces by a length R_f on one side after the rupture; and, if a is the thickness of the vanished film, then $E_M = \rho v_{rim}^2 a R_f$, where v_{rim} is the rim-retraction velocity. If we assume, furthermore, that the rim retracts with a constant velocity, then $dv_{rim}/dt = 0$, so $dR_f/dt = v_{rim}$. Finally, we find

$$\sigma dS(t)/dt \propto dE_M/dt, \Rightarrow v_{rim} = (\sigma/\rho)^{1/2}. \quad (7)$$

This dependence of v_{rim} on σ matches the experimental observations in Ref. [21]. Moreover, this dependence is the same in both our CHNS and VoF DNSs, even though, in the former, antibubble breakup occurs because of gravity-induced thinning, whereas, in the latter, this breakup is induced by puncturing the antibubble at its bottom boundary. The puncturing initial condition has also been used in the experiments and a theory of antibubble collapse [22, 23].

The plot in Fig. 3(b) shows that rim velocities, which we obtain from 2D CHNS and VoF DNSs and our 3D axisymmetric VoF runs, for both high and low A , are in excellent agreement with the theoretical prediction $v_{th} \sim \sqrt{\sigma/\rho_2 a}$ [23], where a is the radius of the rim ($\sqrt{h_0 R_0/\pi}$).

D. Energy time series

When an antibubble bursts, the surface tension energy is converted into the kinetic energy of the fluid; this yields a spike in the fluid-energy time series (see Fig. 4(a)). Therefore, we identify the breakup time τ_1 as the instant at which $dE(t)/dt$ displays a maximum. We also define the breakup time τ_2 at which the antibubble-shell thickness h_{min} , at the lower end of the antibubble, vanishes. In Fig. 4(b) we show plots of both τ_1 and τ_2 versus Bo for an antibubble with $R_0/h_0 = 11$ and $\nu = 0.967$. This plot shows that both our estimates of the collapse times, τ_1 and τ_2 , agree with each other. (For details, see the Supplemental Material [41].)

E. Antibubble-breakup times

The antibubble-breakup times, which we have defined above, depend on the initial size of the antibubble, the surface tension, and the kinematic viscosity. We explore these dependences below via our 2D CHNS DNSs.

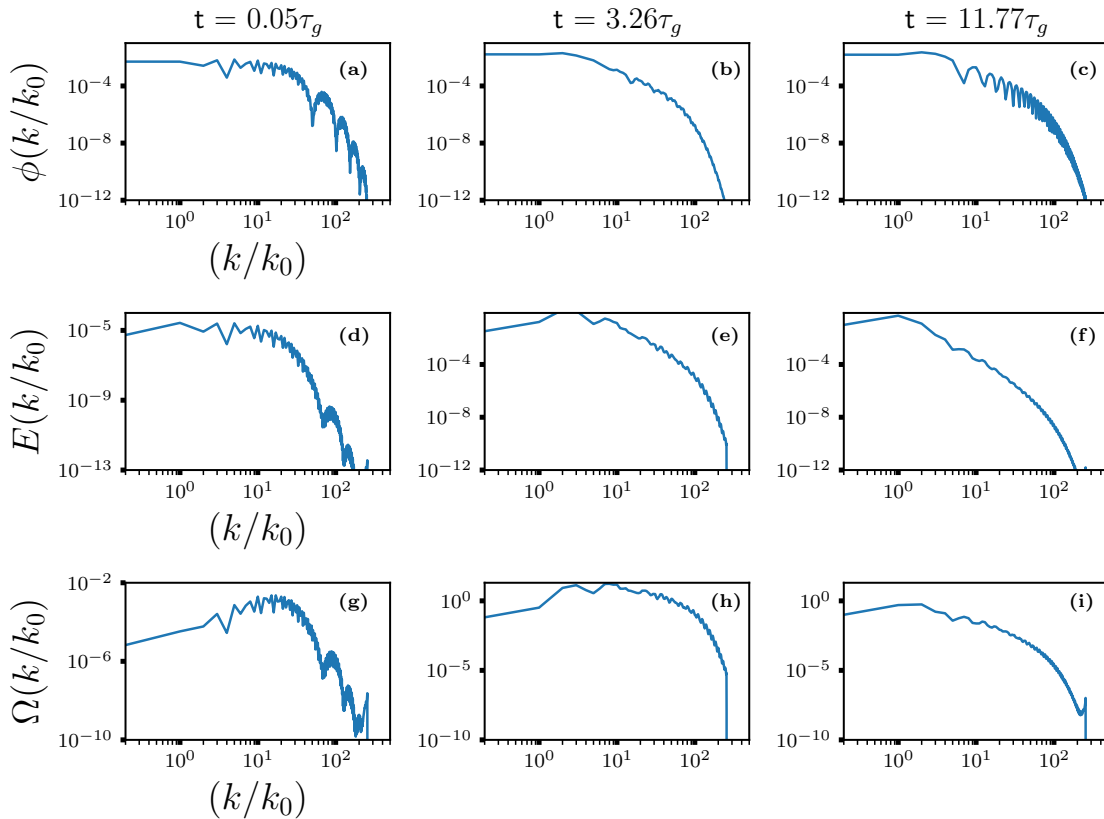


FIG. 2. Log-log (base 10) plots of the spectra (Eq. 6) (a)–(c) $S(k, t)$, (d)–(f) $E(k, t)$, and (g)–(i) $\Omega(k, t)$ versus k , with $k_0 = 1$ and time in units of τ_g .

1. Dependences on Size and Surface Tension

The size- and surface-tension dependences of the antibubble-breakup time follow from the plots of τ_1/τ_g versus Bo , which we give in Fig. 4(d), for (i) $R_0/h_0 = 9$ (DNS runs R13–R16, pink line with triangles), (ii) $R_0/h_0 = 8$ (DNS run R17–R20, red line with squares), and (iii) $R_0/h_0 = 9$ (DNS run R21–R24, blue line with circles). In all these plots, the viscosity is fixed and the Schmidt number $Sc = 1.75$. Although the scaling of τ_1 by $\tau_g = \sqrt{R/Ag}$ makes all the curves collapse on top of each, to a large degree, there is a small, but noticeable, difference between these curves.

2. Dependence on the kinematic viscosity

In Fig. 4(e), we present a log-log plot of τ_1/τ_g versus Sc , over three orders of magnitude and at a fixed value of Bo ; clearly, τ_1/τ_g increases with Sc , with low- Sc and high- Sc asymptotes, which are consistent with $Sc^{1/3}$ and $Sc^{2/3}$.

In Fig. 4(f), we plot h_{min} versus t/τ_g , at $Bo = 1.85 \times 10^{-4}$ and $A = 0.01$ and $g = 99$, for $Sc = 1.75$ (blue line with triangles), $Sc = 66$ (red line with diamonds), and

$Sc = 245$ (yellow line with crosses). We note that h_{min} falls rapidly, for $Sc = 1.75$, but falls slowly, when $Sc = 5.75$. This observation agrees with experiments [21].

F. Three-dimensional antibubbles

We now present illustrative results for 3D antibubbles evolving under gravity from our CHNS and VoF runs Q1–Q7, in Table III, and APR1–APR14, in Table IV, respectively. In Fig. 5 (a) we give, for comparison, an image of an antibubble from an experiment (courtesy of C. Kalelkar from Ref. [12]). In Figs. 5 (b) and (c) we show pseudocolor plots of two-dimensional sections of ϕ (with $y = \pi$ in our 3D CHNS run R2) at (b) $t = 0.1\tau_g$, and (c) $t = 0.3\tau_g$. These plots show clearly the how the South pole of the antibubble becomes thinner, with the passage of time, while a dome develops at its North pole. We also find that, at least for the parameters we use, the initially spherical antibubble remains axisymmetric. Therefore, we design our 3D VoF simulations to be axisymmetric. In Figs. 5 (d)–(e) we show the rupture of an antibubble in our 3D axisymmetric APR7 VoF run at (d) $t = 0$, (e) $t = 0.1\tau_g$, and (f) $t = 0.3\tau_g$.

As we did in our 2D CHNS studies, we identify the

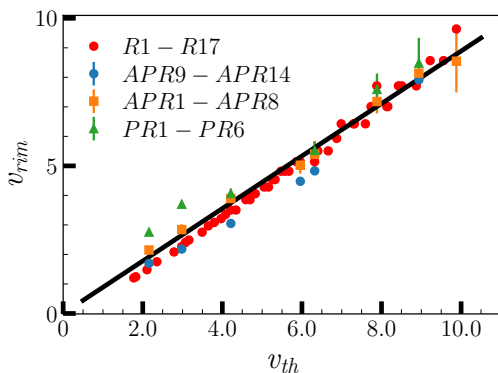


FIG. 3. Plot of the retraction velocity v_{rim} versus the theoretical estimate $v_{th} = \sqrt{\sigma/\rho_2 a}$ for our 2D CHNS runs R1-R17, 2D VoF runs PR1-PR6, and 3D axisymmetric VoF runs APR1-APR14; red circles show data from our CHNS runs; green, yellow, and blue markers indicate data from our VoF runs. The black line represents the theoretical line. Here the surface tension $\sigma = \frac{Ag\rho h_0^2}{Bo}$, where Bo is the Bond number.

antibubble-breakup time τ_1 as the time when dE/dt reaches its maximum value. In Fig. 5(f) we plot τ_1/τ_g versus Bo for our 3D CHNS runs Q1-Q6; we find that this plot is qualitatively similar to its 2D CHNS counterpart in Fig. 4(b). We recall that the plot in Fig. 3(b) also shows that rim velocities, which we obtain from 3D axisymmetric VoF runs, are in excellent agreement with the theoretical prediction [23].

IV. CONCLUSIONS

An experimental study [7] has the title *Vita brevis of antibubbles*. We have shown how to use the CHNS system for studying the spatiotemporal evolution of this short life of antibubbles, in both 2D and 3D. Our DNSs of the CHNS system allow us to study, numerically and theoretically, the collapse or breakup of an antibubble because of the gravity-induced thinning at its South pole. This occurs in experiments via the drainage of air from the lower end of the antibubble. In some experiments, where antibubbles are stabilised, say by the addition of surfactants, antibubble rupture is precipitated by piercing its shell; we have studied such rupture via the VoF method.

By considering Fourier-space spectra, we have shown that the breakup of an antibubble leads to turbulence, insofar as these spectra have significant weight over several orders of magnitude of wavenumbers. Our DNSs have allowed us to study the dependence of the antibubble lifetime on the surface tension, which is related inversely to the Bond number Bo , the kinematic viscosity, which is related directly to the Schmidt number Sc , and the ratio R_0/h_0 of the initial antibubble radius R_0 and its thickness h_0 . We have also shown how the antibubble-rim-retraction velocity depends on the surface tension, in both CHNS and VoF DNSs.

The dependence of the antibubble lifetime on the surface tension has been studied earlier [21], through experiments and numerical simulation of the balance equations obtained from lubrication theory. A recent study [24] uses the Allen-Cahn-Navier-Stokes equations, with order-parameter conservation enforced numerically via a Lagrange multiplier. Our work extends significantly theoretical and DNS studies of antibubbles, by using the CHNS system, in which order-parameter conservation is built in manifestly, and the VoF method that can be used fruitfully if interfaces are very thin and non-Boussinesq effects are present. Our results agree with earlier results, where they exist. The number of studies on antibubbles is limited partly because great care has to be exercised to stabilize antibubbles in terrestrial (as opposed to zero-gravity) experiments. Often a surfactant has to be introduced into the high-density liquid phase for such stabilization. We hope our detailed study of the spatiotemporal evolution of antibubbles, from their initiation to their rupture, and of their effect on the background fluid, will lead to more experimental studies of the properties of these ephemeral, but beautiful, inverted bubbles.

ACKNOWLEDGMENTS

We thank Chirag Kalelkar for introducing us to experimental studies of antibubbles and for the image in Fig. 5 (a) from his experiments [12]. We thank Nadia Bihari Padhan and Sumantra Sarkar for discussions. NP thanks Los Alamos National Laboratory for support; PP and RR acknowledge support from intramural funds at TIFR Hyderabad from the Department of Atomic Energy (DAE), India and DST (India) Project No. ECR/2018/001135; RP thanks CSIR and DST (India) for support and SERC (IISc) for computational resources.

[1] W. Hughes and A.R. Hughes, “Liquid drops on the same liquid surface,” *Nature* **129**, 59 (1932).
 [2] S. Kotopoulis, A. Delalande, M. Popa, V. Mamaeva, G. Dimcevski, O.H. Gilja, M. Postema, B. Tore Gjertsen, and E. McCormack, “Sonoporation-enhanced chemotherapy significantly reduces primary tumour burden in an orthotopic pancreatic cancer xenograft,” *Molecular imaging and biology* **16**, 53–62 (2014).

[3] K. Johansen, S. Kotopoulis, A.T. Poortinga, and M. Postema, “Nonlinear echoes from encapsulated antibubbles,” *Physics Procedia* **70**, 1079–1082 (2015).
 [4] S. Kotopoulis, K. Johansen, O.H. Gilja, A.T. Poortinga, and M. Postema, “Acoustically active antibubbles,” *Dynamics* **2**, 9 (2015).

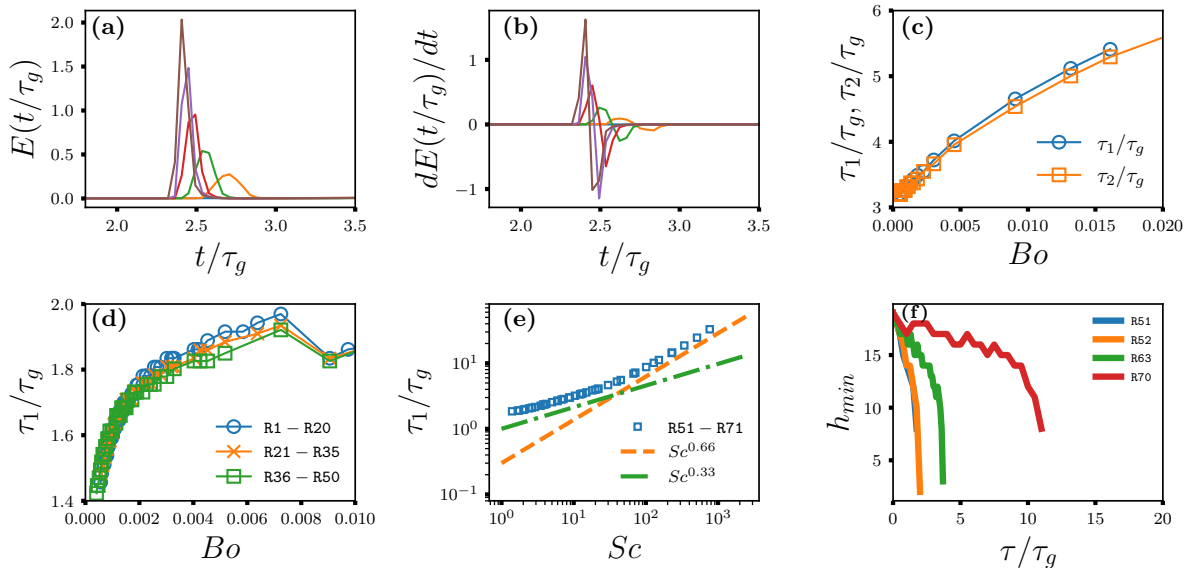


FIG. 4. Plots of (a) the total kinetic energy $E(t)$ and (b) the time derivative $dE(t)/dt$ versus t/τ_g for the 2D CHNS runs R16–R20; (c) plots versus Bo of the antibubble lifetimes τ_1 and τ_2 calculated, respectively, from the energy time series (blue line with circles) and the minimum antibubble thickness (orange line with squares), for the 2D CHNS runs R1–R16. (d) Plots versus Bo (for $Sc = 1.75$), of τ_1/τ_g for $R_0/h_0 = 7$ (DNS run R1–R20, blue line with circles), $R_0/h_0 = 8$ (DNS run R21–R35, orange line with crosses), $R_0/h_0 = 9$ (DNS run R36–R50, green line with squares); (e) log-log plot of τ_1/τ_g versus Sc , over three orders of magnitude and at a fixed value of Bo (runs R51–R71); (f) plots of h_{min} versus t/τ_g , at $Bo = 0.01$ and $A = 0.01$ and $g = 99$, for $Sc = 1.75$ (R51, blue line), $Sc = 1.75$ (R52, orange line) $Sc = 20$ (R63, green line), and $Sc = 151.5$ (R70, red line).

- [5] Michiel Postema and Odd H Gilja, “Ultrasound-directed drug delivery,” *Current pharmaceutical biotechnology* **8**, 355–361 (2007).
- [6] Kristoffer Johansen, Spiros Kotopoulos, and Michiel Postema, “Ultrasonically driven antibubbles encapsulated by newtonian fluids for active leakage detection,” (2015).
- [7] Stéphane Dorbolo, Nicolas Vandewalle, Etienne Reyssat, and David Quéré, “Vita brevis of antibubbles,” *Europhysics News* **37**, 24–25 (2006).
- [8] P Geon Kim and Jerusha Vogel, “Antibubbles: factors that affect their stability,” *Colloids and Surfaces A: Physicochemical and Engineering Aspects* **289**, 237–244 (2006).
- [9] Stéphane Dorbolo, Denis Terwagne, R Delhalle, J Du Jardin, N Huet, N Vandewalle, and N Denkov, “Antibubble lifetime: influence of the bulk viscosity and of the surface modulus of the mixture,” *Colloids and Surfaces A: Physicochemical and Engineering Aspects* **365**, 43–45 (2010).
- [10] S. Dorbolo, H. Caps, and N. Vandewalle, “Fluid instabilities in the birth and death of antibubbles,” *New J. of Phys.* **5**, 161 (2003).
- [11] Lixin Bai, Weilin Xu, Pengfei Wu, Weijun Lin, Chao Li, and Delong Xu, “Formation of antibubbles and multilayer antibubbles,” *Colloids and Surfaces A: Physicochemical and Engineering Aspects* **509**, 334–340 (2016).
- [12] Chirag Kalelkar, “The inveterate tinkerer,” *Resonance* **22**, 955–960 (2017).
- [13] Emmanouil Chatzigiannakis, Nick Jaensson, and Jan Vermant, “Thin liquid films: where hydrodynamics, capillarity, surface stresses, and intermolecular forces meet,” *Current Opinion in Colloid & Interface Science*, 101441 (2021).
- [14] Emmanouil Chatzigiannakis and Jan Vermant, “Breakup of thin liquid films: From stochastic to deterministic,” *Physical Review Letters* **125**, 158001 (2020).
- [15] Youngsup Song, Lenan Zhang, and Evelyn N Wang, “Criteria for antibubble formation from drop pairs impinging on a free surface,” *Physical Review Fluids* **5**, 123601 (2020).
- [16] Jelle B Will, Varghese Mathai, Sander G Huisman, Detlef Lohse, Chao Sun, and Dominik Krug, “Kinematics and dynamics of freely rising spheroids at high reynolds numbers,” *Journal of Fluid Mechanics* **912** (2021).
- [17] Yanshen Li, Christian Diddens, Andrea Prosperetti, and Detlef Lohse, “Marangoni instability of a drop in a stably stratified liquid,” *Physical Review Letters* **126**, 124502 (2021).
- [18] Álvaro Moreno Soto, Pablo Peñas, Guillaume Lajoinie, Detlef Lohse, and Devaraj van der Meer, “Ultrasound-enhanced mass transfer during single-bubble diffusive growth,” *Physical Review Fluids* **5**, 063605 (2020).
- [19] Álvaro Moreno Soto, Detlef Lohse, and Devaraj van der Meer, “Diffusive growth of successive bubbles in confinement,” *Journal of fluid mechanics* **882** (2020).
- [20] Vivek N Prakash, J Martínez Mercado, Leen van Wijngaarden, Ernesto Mancilla, Yoshiyuki Tagawa, Detlef Lohse, and Chao Sun, “Energy spectra in turbulent bubbly flows,” *Journal of fluid mechanics* **791**, 174–190 (2016).
- [21] B. Scheid, S. Dorbolo, L.R. Arriaga, and E. Rio, “An-

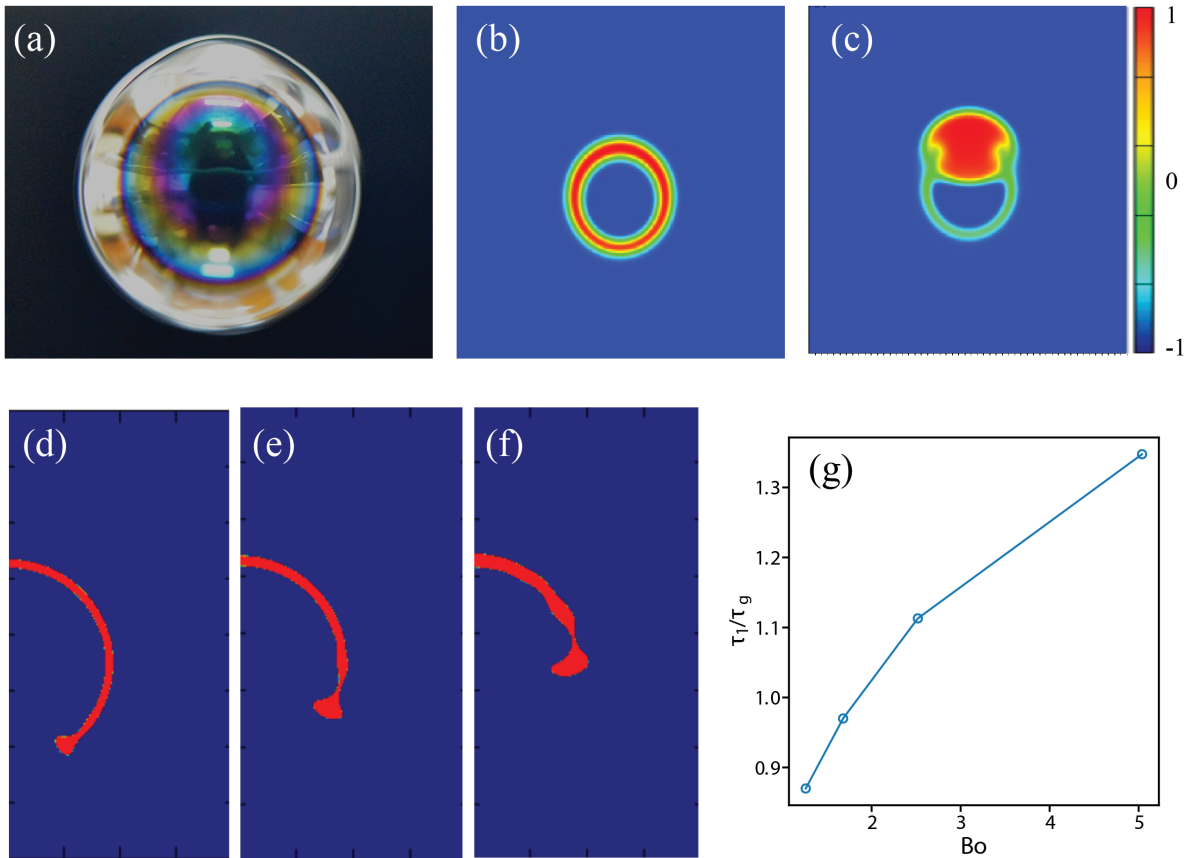


FIG. 5. (a) Image from an antibubble experiment [12]; pseudocolor plot of order parameter showing a section at $y = \pi$ from 3D simulations of antibubbles from run R2 at (b) $t = 0.1\tau_g$ and (c) $t = 0.3\tau_g$; Pseudocolor plots of ϕ from our 3D axisymmetric VoF run APR7 run at (d) $t = 0$, (e) $t = 0.1\tau_g$ (f), and $t = 0.3\tau_g$ showing majority (blue) and minority (red) phases; (g) plot of τ_1/τ_g versus Bo from our 3D CHNS runs Q1-Q6.

tibubble dynamics: The drainage of an air film with viscous interfaces,” *Phys. Rev. Lett.* **109**, 264502 (2012).

- [22] J. Zou, C. Ji, B.G. Yuan, X.D. Ruan, and X. Fu, “Collapse of an antibubble,” *Phys. Rev. E* **87**, 061002 (2013).
- [23] D.N. Sob’yanin, “Theory of the antibubble collapse,” *Phys. Rev. Lett.* **114**, 104501 (2015).
- [24] Junxiang Yang, Yibao Li, Darae Jeong, and Junseok Kim, “Mathematical modeling and simulation of antibubble dynamics,” *NUMERICAL MATHEMATICS-THEORY METHODS AND APPLICATIONS* **13**, 81–98 (2020).
- [25] Youen Vitry, Stéphane Dorbolo, Jan Vermant, and Benoit Scheid, “Controlling the lifetime of antibubbles,” *Advances in colloid and interface science* **270**, 73–86 (2019).
- [26] Guido Boffetta and Robert E Ecke, “Two-dimensional turbulence,” *Annual Review of Fluid Mechanics* **44**, 427–451 (2012).
- [27] Prasad Perlekar, Roberto Benzi, Herman JH Clercx, David R Nelson, and Federico Toschi, “Spinodal decomposition in homogeneous and isotropic turbulence,” *Physical review letters* **112**, 014502 (2014).
- [28] Luca Scarbolo, Dafne Molin, Prasad Perlekar, Mauro Sbragaglia, Alfredo Soldati, and Federico Toschi, “Unified framework for a side-by-side comparison of different multicomponent algorithms: Lattice boltzmann vs. phase field model,” *Journal of Computational Physics* **234**, 263–279 (2013).
- [29] N. Pal, P. Perlekar, A. Gupta, and R. Pandit, “Binary-fluid turbulence: Signatures of multifractal droplet dynamics and dissipation reduction,” *Phys. Rev. E* **93**, 063115 (2016).
- [30] Prasad Perlekar, Nairita Pal, and Rahul Pandit, “Two-dimensional turbulence in symmetric binary-fluid mixtures: Coarsening arrest by the inverse cascade,” *Scientific Reports* **7**, 44589 (2017).
- [31] John D Gibbon, Nairita Pal, Anupam Gupta, and Rahul Pandit, “Regularity criterion for solutions of the three-dimensional cahn-hilliard-navier-stokes equations and associated computations,” *Physical Review E* **94**, 063103 (2016).
- [32] J.D. Gibbon, A. Gupta, N. Pal, and R. Pandit, “The role of bkm-type theorems in 3d euler, navier–stokes and cahn–hilliard–navier–stokes analysis,” *Physica D* **376–377**, 60–68 (2018).
- [33] Xiang Fan, PH Diamond, L Chacón, and Hui Li, “Cas-

- cares and spectra of a turbulent spinodal decomposition in two-dimensional symmetric binary liquid mixtures,” *Physical Review Fluids* **1**, 054403 (2016).
- [34] Xiang Fan, PH Diamond, and Luis Chacón, “Formation and evolution of target patterns in cahn-hilliard flows,” *Physical Review E* **96**, 041101 (2017).
- [35] Xiang Fan, PH Diamond, and L Chacón, “Chns: A case study of turbulence in elastic media,” *Physics of Plasmas* **25**, 055702 (2018).
- [36] A. Celani, A. Mazzino, P. Muratore-Ginanneschi, and L. Vozella, “Phase-field model for the rayleigh–taylor instability of immiscible fluids,” *J. Fluid Mech.* **622**, 115–134 (2009).
- [37] L. Scarbolo and A. Soldati, “Turbulence modulation across the interface of a large deformable drop,” *J. Turbulence* **14**, 27–43 (2013).
- [38] P. Yue, J.J. Feng, C. Liu, and J. Shen, “A diffuse-interface method for simulating two-phase flows of complex fluids,” *J. Fluid Mech.* **515**, 293–317 (2004).
- [39] L. Scarbolo, D. Molin, and A. Soldati, “Phase field model simulation of droplet deformation and breakup in wall bounded turbulence,” in *APS Division of Fluid Dynamics Meeting Abstracts* (2011).
- [40] Rahul Pandit, Prasad Perlekar, and Samriddhi Sankar Ray, “Statistical properties of turbulence: an overview,” *Pramana* **73**, 157 (2009).
- [41] “Attached supplementary material.”
- [42] C. Canuto, M.Y. Hussaini, A. Quarteroni, A. Thomas Jr, et al., *Spectral methods in fluid dynamics* (Springer Science & Business Media, 2012).
- [43] S.M. Cox and P.C. Matthews, “Exponential time differencing for stiff systems,” *J. Comp. Phys.* **176**, 430–455 (2002).
- [44] http://www.nvidia.com/object/cuda_home_new.html..
- [45] <http://basilisk.fr..>
- [46] Stéphane Popinet, “Numerical models of surface tension,” *Annu. Rev. Fluid Mech.* **50**, 1–28 (2018).
- [47] John B Bell, Phillip Colella, and Harland M Glaz, “A second-order projection method for the incompressible navier-stokes equations,” *Journal of Computational Physics* **85**, 257–283 (1989).